THE JOURNAL OF PHYSICAL CHEMISTRY Letters

Perspective

Cite This: J. Phys. Chem. Lett. 2019, 10, 5805−5814

pubs.acs.org/JPCL

Frequency-, Time-, and Wavevector-Resolved Ultrafast Incoherent Diffraction of Noisy X-ray Pulses

Shahaf Asban,*,†,‡ Daeheum Cho,*,†,‡ and Shaul Mukamel*,†

†Department of Chemistry and Physics and Astronomy, University of California, Irvine, California 92697-2025, United States

Supporting Information

ABSTRACT: We study theoretically incoherent time-resolved X-ray diffraction of fluctuating sources such as free electron lasers, as well as coherent sources with controllably added randomness. We find that the temporal resolution is strongly eroded by the noise. By considering frequency resolution of the signal, we find that the statistical properties of the noise carry important information allowing us to restore the temporal resolution. We propose a multidimensional stochastic resonance treatment to shape the optical window and extract this information from signals. Using the frequency-dependent stochastic phase as a frequency marker allows to improve the spectral resolution as well via intensity correlations. Frequency-tuned field correlation functions are used to modify the effective frequency gating and extract specific charge density contributions to the diffraction pattern while maintaining temporal resolution.

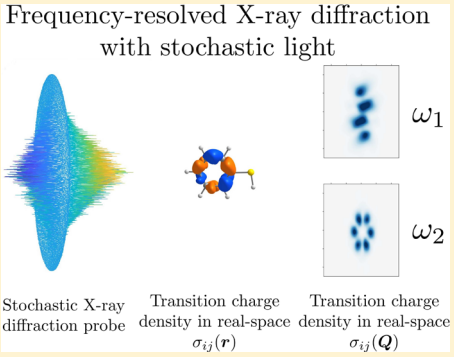

Incoherence of light sources is usually regarded as a disadvantage because it can erode desirable spectroscopic features. However, stochastic characteristics can become a useful resource for controlling the interplay of spectral and temporal resolutions. The stochastic properties of new generation X-ray free electron laser sources have attracted considerable attention.[1,2] The randomness can also be added to a coherent source, creating a controlled noise distribution.[3] Understanding the role of the statistical characteristic of light is crucial for the interpretation of spectroscopic and diffraction experiments.

Spectral information on matter is commonly acquired by resonant peaks in its response to electromagnetic radiation. These peaks are located at the transition frequencies and broadened by dissipation caused by finite excitation lifetimes and thermal fluctuations. These resonances are an elementary frequency-domain manifestation of the propagation of intertwined matter and light waves. Off-resonant X-ray diffraction patterns encode geometric information on the sample, i.e., its structure and the spatial distribution of charge. The structural information is carried by the momentum scattering wavevector $\boldsymbol{Q} = \boldsymbol{k}_s - \boldsymbol{k}_p$, where $\boldsymbol{k}_s$ and $\boldsymbol{k}_p$ represent the scattered and incident waves, respectively. The $\boldsymbol{Q}$-dependent intensity of the diffraction pattern is modulated by the interference of waves due to the charge density profile of each scatterer (short wavelength, high $\boldsymbol{Q}$), resulting in the diffraction pattern $S(\boldsymbol{Q}) \propto |\sigma(\boldsymbol{Q})|^2$, where $\sigma(\boldsymbol{Q})$ is the charge-density. Combining the spatial and frequency resolutions offers a powerful window into matter dynamics.

Bright ultrashort X-ray pulses produced by free electron lasers (FELs) can monitor electronic and vibrational dynamics at molecular (or atomic) time and length scales.[4−6] These sources are usually based on the self-amplified spontaneous emission (SASE) process, which generates strongly fluctuating stochastic radiation produced by bunched electrons shot-noise.[7] The temporal profile then varies considerably from pulse to pulse. Moreover, SASE pulses are characterized by many longitudinal modes which are not phase-locked. They provide high first-order spatial coherence[8,9] yet are statistically chaotic in higher orders.[7,10] Accounting for the randomness is crucial for the interpretation of spectroscopic measurements and the restoration of the eroded temporal resolution. Stochastic radiative spectral-temporal profiles can be further shaped and controlled.[11] Stochastic systems may also show new resonances (see ref 12 for a comprehensive review). Shaped noise characteristics may further be used as a powerful control knob. By recording the signal for each noisy realization of the pulse, it is possible to postprocess higher-order quantities using the same data. Stochastic properties of radiation have long been used to extract extra spectroscopic information not available by coherent light. Early studies utilized the short correlation time to mimic ultrafast pulses and thus constitute a poor man's femtosecond measurement using noisy nanosecond pulses[13−16] and appendix 10B of ref 17. Covariance analysis of stimulated X-ray Raman signals

Frequency dispersion of time-resolved X-ray diffraction, apart from being interesting in its own right, can further restore the temporal resolution.

Received: April 1, 2019
Accepted: September 10, 2019
Published: September 10, 2019

DOI: 10.1021/acs.jpclett.9b00924
J. Phys. Chem. Lett. 2019, 10, 5805−5814

obtained using noisy SASE sources has been used to unravel spectral information out of noisy data.[1−3,18]

In this Perspective we develop the statistical approach to *wavevector-, time-, and frequency-resolved diffraction* signals and present a multidimensional stochastic imaging framework, based on high statistical moments of the acquired data and the incoming radiation. Our main finding suggests that frequency dispersion of time-resolved X-ray diffraction, apart from being interesting by its own virtue, can further restore the temporal resolution. The time scale in such experiments is set by the pump−probe delays, and fast oscillations are exponentially suppressed by phase fluctuations. We further propose to use stochastic sources to enhance the spectral resolution at the expense of the temporal resolution. These results are illustrated by simulations of diffraction from thiophenol. The molecule is first prepared in a nonstationary electronic wavepacket by an actinic pulse, followed by the diffraction of a probe pulse at variable delays.

In the absence of long-range order, the signal is given by an incoherent sum of single-molecule contributions. The frequency-dispersed X-ray diffraction pattern, originating from the interaction of light with matter, is given by[19]

$$S(\omega_s, t_s, \boldsymbol{k}_s, \boldsymbol{r}_s) = \int \mathrm{d}\boldsymbol{r}\, \mathrm{d}t \left\langle \boldsymbol{E}^{\dagger(trfk)}(\boldsymbol{r}, t)\boldsymbol{E}^{(trfk)}(\boldsymbol{r}, t) \exp\left[-\frac{\mathrm{i}}{\hbar}\int_{-\infty}^{t} \mathrm{d}\tau \mathcal{H}_{I-}(\tau)\right]\right\rangle \tag{1}$$

where $\boldsymbol{E}^{(trfk)}$ is the temporally and spectrally gated electric field operator given in the Supporting Information and the superoperator O_- action on a Hilbert space operator A is defined by the commutator $O_-A = OA - AO$. Off-resonant diffraction is caused by the minimal coupling radiation/matter Hamiltonian

$$\mathcal{H}_I = \int \mathrm{d}\boldsymbol{r}\, \hat{\sigma}(\boldsymbol{r}, t)\hat{\boldsymbol{A}}^2(\boldsymbol{r}, t) \tag{2}$$

where $\boldsymbol{A}$ is the vector potential and $\hat{\sigma}$ is the electron-density operator. The diffraction to second order in $\mathcal{H}_I$ is depicted in Figure 1. The shaded area represents an arbitrary preparation of a valence electronic wavepacket by an actinic pulse, initially in the ground state.

We demonstrate how to extract desired information regarding excited states, separated from the dominant ground-state contribution to frequency-resolved diffraction, further enhanced by statistical postprocessing. We follow the derivation in ref 19. We assume high spatial resolution

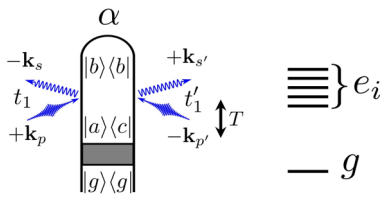

Figure 1. Single-molecule diffraction process. The shaded area represents the preparation of an electronic wavepacket. We consider two types of possible preparation schemes. An optical pulse prepares a nuclear wave packet in an electronic excited state. An X-ray Raman process creates a broad superposition of electronic wave packet. Here, g and e_i represent the ground and excited states, respectively. a, b, and c represent any electronic state, i.e., g or e_i.

considering ideal gating $R(\boldsymbol{r}, \boldsymbol{r}') = \delta(\boldsymbol{r} - \boldsymbol{r}')$ corresponding to a vanishing pixel size (see appendix A in the Supporting Information). We further assume impulsive pulses, which fixes the interaction time around a controlled delay period T. The frequency resolution is determined by the spectral window $F(\omega_s,\bar{\omega}_s)$, where $\bar{\omega}_s$ is the detected frequency. We focus on the second-order process depicted in Figure 1 and consider four variants of single-molecule diffraction of plane waves as summarized in Table 1.The time-resovled X-ray diffraction is given by

$$S_{\mathrm{TRXD}}(\boldsymbol{Q}, T) = \kappa \sum_{abc} \rho_{ac}(T)\sigma_{ba}[\boldsymbol{Q}]\sigma_{bc}^{*}[\boldsymbol{Q}] \tag{3}$$

where $\boldsymbol{Q} = \boldsymbol{k}_s - \boldsymbol{k}_p$ is the diffraction wavevector sampled at the detection plane. Second, the time- and frequency-resolved diffraction is S_{FTRXD}[20]

$$S_{\mathrm{FTRXD}}(\bar{\omega}_s, \boldsymbol{Q}, T; \Lambda) = NK \int \mathrm{d}\omega_s \omega_s^2 G(\omega_s, \bar{\omega}_s)\omega_s^2 \sum_{abc} \rho_{ac}(T) \times \sigma_{ba}[\boldsymbol{Q}(\omega_s)]\sigma_{bc}^{*}[\boldsymbol{Q}(\omega_s)]\langle A_p(\omega_s + \omega_{ba})A_p^{*}(\omega_s + \omega_{bc})\rangle_\Lambda \tag{4}$$

from which we will study the role of the stochastic components and reduced temporal resolution. Here, Λ denotes collectively the stochastic light parameters and $\langle\cdots\rangle_\Lambda$ represents averaging over an ensemble of noise realizations; $G(\omega_s,\bar{\omega}_s)$ is the spectral window (see the Supporting Information) around the measured frequency $\bar{\omega}_s$. The third variant given in eq 5 is the covariance of the frequency-resolved diffraction (eq 4), with the Fourier transform of the *time-resolved* intensity of the noisy probe. We show that with proper choice of frequencies, the temporal resolution is restored, overcoming the noise. The fourth variation of this signal given in eq 12 is based on covariance calculation of the frequency resolved diffraction in eq 4, with the Fourier transform of two *time-resolved* field components of the probe. We stress that the field is measured in the *time domain* only once for each repetition of the experiment. We show that with special choice of Fourier components, the time−frequency resolution spectral window may be controlled, and desired contributions to the diffraction pattern can be isolated.

We show that with special choice of Fourier components, the time−frequency resolution spectral window may be controlled, and desired contributions to the diffraction pattern can be isolated.

To describe the stochastic radiation, be it by design or because of a nonideal source, we introduce a frequency-dependent random phase $\boldsymbol{A}_p(\omega) \equiv A(\omega)\exp\{\mathrm{i}\lambda\varphi[\omega]\}$, where λ is the stochasticity strength parameter. $\varphi[\omega]$ may vary slowly with ω in each realization of the pulse, but it exhibits strong fluctuations between different realizations. When two frequencies are coupled through interaction with matter, say a Raman process, these frequencies in the signal will be correlated. Because diffraction involves two interactions with the pulse, the correlation introduced by frequencies that are

DOI: 10.1021/acs.jpclett.9b00924
J. Phys. Chem. Lett. 2019, 10, 5805−5814

Table 1. Summary of the Available Features of the Diffraction Techniques Discussed in the Perspective

diffraction technique	advantage	limitation
TRXD (eq 3)	captures the time-dependent features	no resolution of different Raman processes
FTRXD (eq 5)	resolve diffraction contributions by Raman frequency	stochasticity attenuate the dynamic information by a factor of $e^{-\sigma^2\lambda^2\lvert\omega_{ca}\rvert}$ (shown in eq 5)
FTRXD−intensity correlation (eq 8)	recover a full dynamic information	effective frequency-gating window limited by the probe bandwidth
FTRXD−field correlation (eq 12)	further frequency resolution with ω_1 and ω_2 resonant to the Ω_{Raman} on each branch of the loop diagram; narrower frequency-gating window $\propto 1/\sigma^2\lambda^2$	effective frequency-gating window limited by the joint probe bandwidth and noise power spectrum

separated by the transition frequencies is sharply peaked, already the average TRXD signal.

The stochastically induced resonances studied below may be classified according to the number of the random phase variables appearing in the signal. A first-order stochastic resonance appears upon the ensemble averaging of eq 4. To incorporate the stochastic resonances into the signal, the averaging procedure takes the form $\langle \exp(-i\lambda\varphi[\omega])\rangle \equiv \int \mathcal{D}\varphi \mathcal{P}[\varphi] e^{-i\lambda\varphi[\omega]} = \widetilde{\mathcal{P}}[\lambda]$, which constitutes the characteristic function of the underlying stochastic process. Assuming a Gaussian distribution with standard deviation σ, the characteristic function is $\langle \exp(i\lambda\phi)\rangle = \exp(-\lambda^2\sigma^2)$. The corresponding exponential averaging of two phase factors along the frequency interval Ω is given by $\widetilde{\mathcal{P}}(\lambda, \Omega) = \exp(-\lambda^2\sigma^2\Omega)$ (appendix C). Finally, the average frequency resolved diffraction reads

$$\mathcal{S}(\bar{\omega}_s, \mathbf{Q}, T) = \kappa_1^{-1}\langle S_{\text{FTRXD}}(\bar{\omega}_s, Q, T; \Lambda)\rangle_\Lambda \propto \sum_{abc} \bar{\rho}_{ac}(T)\sigma_{ab}(Q)\sigma_{cb}^*(Q)\overline{\boldsymbol{A}_{ab}^s \boldsymbol{A}_{cb}^{s*}} \exp[i\omega_{ac}T - \sigma^2\lambda^2\lvert\omega_{ca}\rvert] \tag{5}$$

where $\kappa_1 = NK$; K is a prefactor given in appendix A, and $\bar{\rho}_{ac}(T) = \rho_{ac}(0)e^{-i\omega_{ac}T}$. We denote the spectrally shifted pump by $\boldsymbol{A}_p(\omega_s + \omega_{ab}) \equiv A_{ab}^s e^{i\lambda\varphi_{ab}^s}$ and the effective spectral window is $\overline{\boldsymbol{A}_{ab}^s \boldsymbol{A}_{cb}^{s*}} = \int d\omega_s\, G(\omega_s, \bar{\omega}_s)\omega^2 \boldsymbol{A}_{ab}^s \boldsymbol{A}_{cb}^{s*}$ We assume that $\sigma_{ab}(\mathbf{Q})$ does not vary significantly across the gating in eq 5 and thus can be considered as a constant $\overline{AA\sigma\sigma} \to \overline{AA}\sigma\sigma$. eq 5 has a maximum for $\omega_{ac} = 0$, which corresponds to the absence of initial coherence. Stronger stochasticity yields sharper resonances in the frequency domain. As shown in eq 5, the stochasticity (σ) provides a frequency-cutoff and attenuates the time-dependent signals from an $|a\rangle\langle c|$ coherence by the factor of $e^{-\sigma^2\lambda^2\lvert\omega_{ca}\rvert}$, while the time-independent contributions from populations remain the same. Equation 5 for values of $|\omega_{ca}|$ is shown in Figure 2. When the time-dependent signal oscillates rapidly with a large $|\omega_{ca}|$, it is hard to retrieve the time-dependent contribution with a stochastic probe pulse.

We next consider a higher-order postprocessing protocol based on measuring the time-resolved intensity of the incident field whose Fourier transform carries the phase fluctuation information for each experimental realization of the pulse. The frequency domain intensity is then given by a correlation function of the fields as shown in appendix B. The diffraction−intensity cross-correlation is defined by

$$\mathcal{S}_{\text{SI}}(\omega_s, \omega_p, \mathbf{Q}, T) = \langle I[\omega_p; \Lambda] S_{\text{FTRXD}}(\omega_s, \mathbf{Q}, T; \Lambda)\rangle_\Lambda / 2\pi\kappa_1 \tag{6}$$

This signal includes contributions which mix the fluctuating phases of the diffraction signal and the pulse intensity.

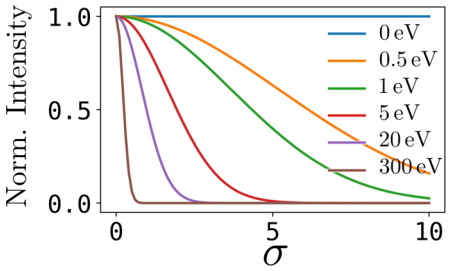

Figure 2. Attenuation of the time-dependent contribution to the average frequency resolved diffraction (eq 5) versus the noise power of the probe pulse σ for various transition frequencies $|\omega_{ca}|$ = 0, 0.5, 1, 5, 20, and 300 eV.

Interestingly, the covariance of this signal does not include the independent phase intervals where the temporal resolution is limited and is given by

$$C_{\text{SI}}(\omega_s, \omega_p, \mathbf{Q}, T) = \langle I[\omega_p; \Lambda] S_{\text{FTRXD}}(\omega_s, \mathbf{Q}, T; \Lambda)\rangle_\Lambda - \langle I[\omega_p; \Lambda]\rangle_\Lambda \langle S_{\text{FTRXD}}(\omega_s, \mathbf{Q}, T; \Lambda)\rangle_\Lambda \tag{7}$$

When $\lambda\sigma\omega_p^{1/2} \gg 1$, the phase-mixing terms are dominant (see the Supporting Information) and the normalized covariance becomes

$$C_{\text{SI}}(\bar{\omega}_s, \omega_p, \mathbf{Q}, T) = \mathcal{A}\sum_{abc} \bar{\rho}_{ac}(T)\sigma_{ba}(\mathbf{Q})\sigma_{bc}^*(\mathbf{Q})\overline{\boldsymbol{A}_{ab}^s \boldsymbol{A}_{cb}^{s*}} e^{i\omega_{ac}T} \tag{8}$$

where $\mathcal{A}$ is the normalization factor. This expression resembles the single-molecule diffraction with coherent light studied in ref 20, and in contrast to eq 5, contains the full temporal dynamics. The stochastic phase thus couples the measured time-resolved intensity frequency components to the diffraction of eq 4. This results in a four-point correlation function (see eq B3 of the Supporting Information) that restores a nonvanishing contribution of the (time-dependent) coherence.

We now introduce another class of signals whereby the frequency dispersed electric field itself (including the phase), rather than the intensity, is recorded for each stochastic realization. This is possible by heterodyne measurement of the incident field with a known reference, with two phases shifted by $\pi/2$. An interesting nonvanishing combination of the random components is found when the diffraction signal eq 4 is correlated with two field amplitudes

$$\mathcal{S}_{S;EE}(\omega_s, \omega_1, \omega_2, \mathbf{Q}, T) = \langle E[\omega_1; \Lambda] S_{\text{FTRXD}}(\omega_s, \mathbf{Q}, T; \Lambda) E^*[\omega_2; \Lambda]\rangle_\Lambda \tag{9}$$

The corresponding covariance $C_{S;EE}$ is given by

DOI: 10.1021/acs.jpclett.9b00924
J. Phys. Chem. Lett. 2019, 10, 5805−5814

$$C_{S;EE}(\omega_s, \omega_1, \omega_2, \mathbf{Q}, T) = \kappa_2^{-1}[\langle E[\omega_1; \Lambda]S_{FTRXD}(\omega_s, \mathbf{Q}, T; \Lambda)E^*[\omega_2; \Lambda]\rangle_\Lambda - \langle E[\omega_1; \Lambda]E^*[\omega_2; \Lambda]\rangle_\Lambda\langle S_{FTRXD}(\omega_s, \mathbf{Q}, T; \Lambda)\rangle_\Lambda] \quad (10)$$

where the prefactor κ_2 is given in appendix B. Similar to eq 7, the phase mixing terms dominate the signal. Because an ensemble average is taken with respect to the stochastic degrees of freedom, one can carry out the calculation of the covariance as an overall addition to the frequency gating. This factor does not vanish only when the averaging interval (ω_1, ω_2) overlaps with ($\omega_s + \omega_{ab}$, $\omega_s + \omega_{cb}$), resulting in the correlation function (see appendix B)

$$\mu_{abc}(\sigma) = \begin{cases} e^{-\lambda^2\sigma^2|\omega_1-\omega_s-\omega_{ab}|}e^{-\lambda^2\sigma^2|\omega_2-\omega_s-\omega_{cb}|}; & \omega_{ca} > 0 \\ e^{-\lambda^2\sigma^2|\omega_2-\omega_s-\omega_{ab}|}e^{-\lambda^2\sigma^2|\omega_1-\omega_s-\omega_{cb}|}; & \omega_{ca} < 0 \end{cases} \quad (11)$$

(for $\omega_2 > \omega_1$ without loss of generality, see the Supporting Information for detailed derivation). By tuning $\omega_1 = \omega_s + \omega_{ab}$ and $\omega_2 = \omega_s + \omega_{cb}$, one can probe the temporal dynamics around these two frequency windows of width $\propto 1/\lambda^2\sigma^2$. This quantifies the frequency−time resolution trade-off for noisy pulses. $C_{S;EE}$ has the structure of a "frequency tweezer" which allows us to suppress or enhance desired contributions with high control. To demonstrate these properties, we break down the contributions of the ground and excited states

$$\begin{aligned} C_{S;EE}(\omega_s, \omega_1, \omega_2, \mathbf{Q}, T) &= \bar{\rho}_{gg}(T)\overline{|\mathbf{A}^s|^2\mu_{ggg}}|\sigma_{gg}(\mathbf{Q})|^2 + \sum_e \bar{\rho}_{gg}(T)\overline{\mu_{geg}|\mathbf{A}^s_{ge}|^2}\,|\sigma_{eg}(\mathbf{Q})|^2 \\ &\quad + \sum_{e_1e_2}\bar{\rho}_{e_1e_2}(T)\overline{\mu_{e_1ge_2}\mathbf{A}^s_{e_1g}\mathbf{A}^{s*}_{e_2g}}\sigma_{e_1g}(\mathbf{Q})\sigma^*_{e_2g}(\mathbf{Q})e^{i\omega_{e_1e_2}T} + \\ &\quad \sum_{e_1e_2e_3}\bar{\rho}_{e_1e_3}(T)\overline{\mu_{e_1e_2e_3}\mathbf{A}^s_{e_1e_2}\mathbf{A}^{s*}_{e_3e_2}}\sigma_{e_1e_2}(\mathbf{Q})\sigma^*_{e_3e_2}(\mathbf{Q})e^{i\omega_{e_1e_3}T} \\ &\quad + 2\mathcal{R}e\left\{\sum_{e_1}\bar{\rho}_{e_1g}(T)e^{i\omega_{e_1g}T}[\overline{\mu_{e_1gg}\mathbf{A}^s_{e_1g}\mathbf{A}^{s*}_{gg}}\sigma_{e_1g}(\mathbf{Q})\sigma^*_{gg}(\mathbf{Q}) + \right. \\ &\quad \left.\sum_{e_2}\overline{\mu_{e_1e_2g}\mathbf{A}^s_{e_1e_2}\mathbf{A}^{s*}_{ge_2}}\sigma_{e_1e_2}(\mathbf{Q})\sigma^*_{ge_2}(\mathbf{Q})]\right\} \end{aligned} \quad (12)$$

where each contribution is associated with a corresponding diagram in Figure 3 and labeled accordingly. We denote the gated correlation function as

$$\overline{\bar{\mu}_{abc}\mathbf{A}^s_{ab}\mathbf{A}^{s*}_{cb}} = \int d\omega_1 F(\bar{\omega}_1, \omega_1)\int d\omega_2 F(\bar{\omega}_2, \omega_2) \times \int d\omega_s\, G(\bar{\omega}_s, \omega_s)\mu_\sigma(\omega_1, \omega_2, \omega_s) \quad (13)$$

To achieve a high frequency resolution, we can use narrow gating functions such that $\bar{\mu}_{abc} = \mu_{abc}(\sigma)$ defined in eq 11. F is determined by the frequency resolution of the measured field.

The key features of the four nonlinear diffraction techniques are summarized in Table 1. The frequency- and time-resolved X-ray diffraction−intensity correlation technique [FTRXD-intensity correlation, $C_{SI}(\bar{\omega}_s, \omega_p, \mathbf{Q}, T)$] can single out desired elastic or inelastic contributions by scanning $\omega_{xs} = \Omega_X - \omega_s$ in resonance with a selected diffraction Raman shift, by varying the detected frequency ω_s while keeping X-ray probe frequency Ω_X fixed. We use the terms elastic and inelastic (Stokes and anti-Stokes) when the signal stems from a diffraction off the population to population $|a\rangle\langle a| \to |b\rangle\langle b|$ (Figure 1A when $a = c$). Only then the Raman frequencies at the two branches of the loop diagram are identical, and the Raman shift can be defined unambiguously. To separate the inelastic from the elastic contributions, a frequency-resolved diffraction pattern can be generated for $\omega_{xs} = 0$. The signal then measures the sum of the elastic contributions ($|g\rangle\langle g| \to |g\rangle\langle g|$ or $|e\rangle\langle e| \to |e\rangle\langle e|$ if $|e\rangle\langle e|$ is populated), while the Stokes and anti-Stokes contributions when $\omega_{xs} > 0$ and $\omega_{xs} < 0$, respectively. Because elastic contributions have a zero Raman shift $\omega_{xs} = 0$, they cannot be further dissected into various contributions by the frequency resolution.

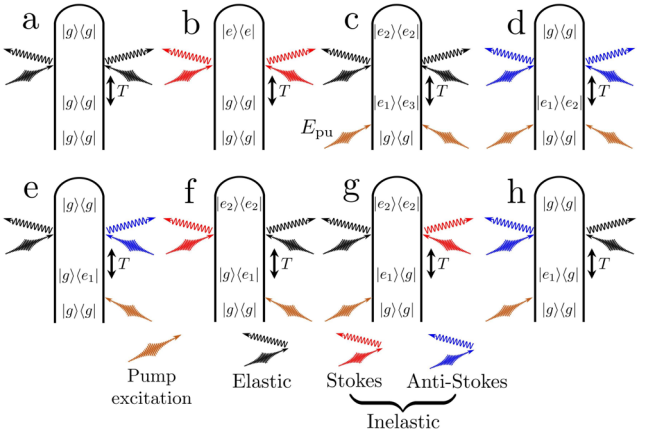

Figure 3. Dissection of the loop diagram for incoherent diffraction of Figure 1 into several diagrams. The same diagram labels are marked in the various terms in eq 12.

When the Raman shifts on the two branches of a loop diagram are different, i.e., a system is in a coherence (Figure 3c−h), in FTRXD-intensity correlation, $\omega_{xs} = (\omega_{ba}+\omega_{bc})/2$ can be set to try to keep $\overline{\mathbf{A}^s_{ab}}$ and $\overline{\mathbf{A}^{s*}_{cb}}$ in the probe bandwidth in eq 8. However, Raman shifts of diffraction processes may be close, which prevents a frequency resolution with ω_{xs}. This issue can be resolved in FTRXD-field correlation, by tuning $\omega_{1s} = \omega_1 - \omega_s$ and $\omega_{2s} = \omega_2 - \omega_s$ in resonance with the Raman shift on the left and right branches of the loop diagram, respectively, on top of tuning ω_{xs}. We can then observe a diffraction event defined by a single loop diagram.

We next demonstrate the information distillation, corresponding to eqs 3, 8, and 12 by numerical simulations for thiophenol, from $|g\rangle\langle g|$ ground-state population, $|e\rangle\langle e|$ excited-state population, $|g\rangle\langle e|$ ground−excited coherence, and $|e\rangle\langle e'|$ excited−excited coherence. Figure 4 shows the setup for the ultrafast X-ray diffraction technique, electronic energy levels and transition dipole moment amplitudes of thiophenol, the actinic pulse envelope $E_{pu}(\omega)$, and the time-evolution of the dominant components of the electronic density matrix (ρ_{ij}). The electronic energy levels $|i\rangle$ relative to the ground state $|0\rangle$ are 6.52, 6.58, 7.73, 8.44, 8.47, 9.28, 9.44, and 10.04 eV. The wave function coefficients for the dominant states at $T = 0$ immediately after an interaction with the actinic pulse are $(c_2(0), c_4(0), c_5(0)) = (6.37, 2.99, 4.43) \times 10^{-3}$, assuming impulsive excitation. The ultrafast X-ray probe pulse is y-polarized (see Figure 4 for the molecular axes).

DOI: 10.1021/acs.jpclett.9b00924
J. Phys. Chem. Lett. 2019, 10, 5805−5814

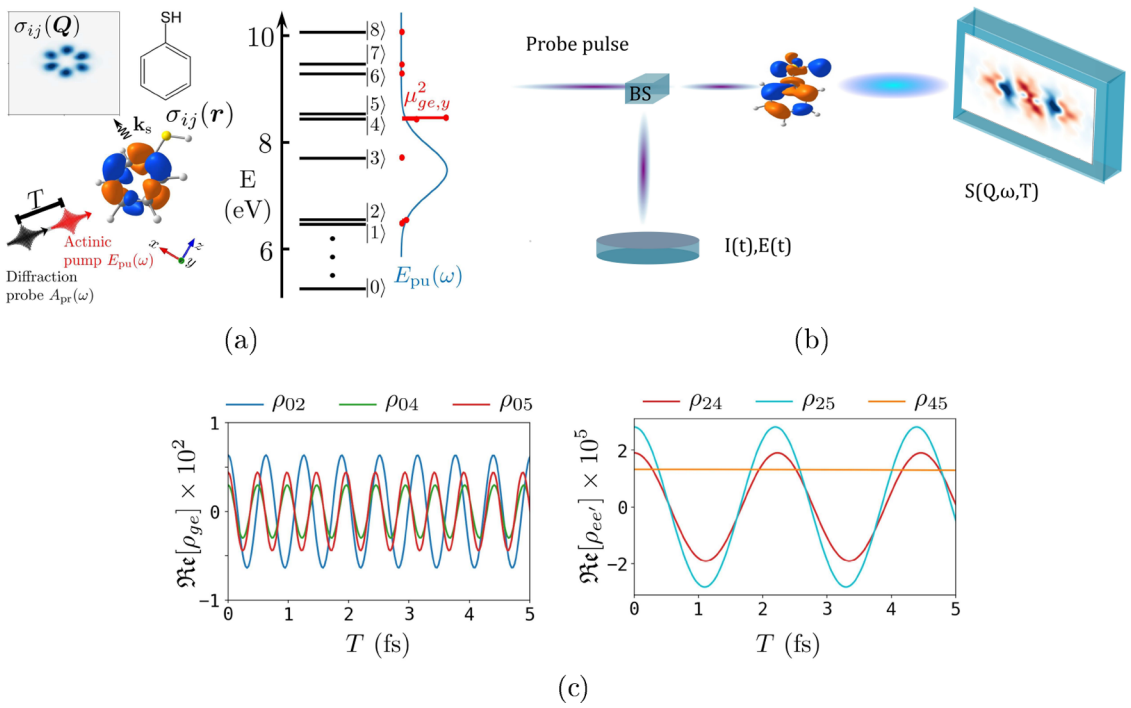

Figure 4. Setup for time-, frequency-, and wavevector-resolved diffraction. (a) Left: Pulse scheme for time-resolved diffraction. The ground-state geometry of the thiophenol. Right: Electronic energy levels in thiophenol. Modulus square of the transition dipole moment in y polarization $\mu^2_{ge,y}$ (red), and the pump-pulse envelope $E_{pu}(\omega)$. (b) Proposed setup including the reference measurements. The noisy probe pulse is time-resolved separately, either intensity (eq 8) or field (eq 10). This reference is used in the postprocessing cross-correlation calculations. (c) Time-evolution of the off-diagonal elements of the electronic density matrix (left) $\mathcal{R}e[\rho_{ge}(T)]$ and (right) $\mathcal{R}e[\rho_{ee'}(T)]$. Transitions between excited states (ee′) are favorable compared to excitations from the ground state, with agreement to the pump spectral window.

Figure 5 shows the elastic and inelastic (Stokes) contributions to the diffraction signals in eqs 3, 8, and 12 from the $|g\rangle\langle g|$ population for different frequencies ω_{xs}. These signals are time-independent as there is no dynamics in the $|g\rangle\langle g|$ population. The signals are proportional to the modulus square of the corresponding transition charge density $S \propto \rho_{gg}|\sigma_{gg}|^2$ or $S \propto \rho_{gg}|\sigma_{ge}|^2$ for the elastic and the Stokes, respectively. In ordinary TRXD displayed in Figure 5 A, the elastic contribution dominates the signal because the diagonal charge density is much larger than the off-diagonal ($\sigma_{ge} \ll \sigma_{gg}$). It is not possible to single out the inelastic contributions.

The FTRXD-intensity correlation depicted in Figure 5B depicts the inelastic Stokes contribution to the charge distribution, free from the elastic scattering that typically dominates the signal. In the left most panel, one can single out the elastic contribution by tuning ($\omega_{xs} = 0$). In the right panels, the Stokes processes corresponding to the $|g\rangle\langle g| \rightarrow |e\rangle\langle e|$ transitions can be resolved by tuning $\omega_{xs} = \omega_{eg} > 0$. The signals are then $S \propto \rho_{gg}|\sigma_{ge}|^2$. By tuning $\omega_{xs} = \omega_{30}$, one can extract the absolute square of the transition charge density from the ground $|0\rangle$ to the third excited state $|3\rangle$. However, if the energy spacing between the two states ω_{ij} is smaller than the X-ray probe pulse bandwidth (0.91 eV), the effective energy windows for different Raman frequencies ω_{xs} (green Gaussian envelopes) overlap and the two contributions are not resolved. To this end, the diffraction signals at $\omega_{xs} = \omega_{10}$ and ω_{20}, and $\omega_{xs} = \omega_{40}$ and ω_{50} are mixtures of the two inelastic contributions due to the small energy spacing ($\omega_{21} = 0.06$ eV and $\omega_{54} = 0.03$ eV).

We next demonstrate the high performance of multidimensional signal−field cross-correlations in enhancing the frequency resolution. Figure 5C shows the signal for increasing noise standard deviation (top, $\sigma = 15$; bottom, $\sigma = 30$) in eq 12 by tuning $\omega_{xs} = \omega_{eg}$, $\omega_{1s} = \omega_1 - \omega_s = \omega_{ge}$ and $\omega_{2s} = \omega_2 - \omega_s = \omega_{ge}$. It is evident that the frequency resolution is enhanced by increasing σ (effective frequency-gating windows are schematically depicted as green Gaussian envelopes in the figure). The Stokes processes stem from the two almost degenerate transitions can be resolved using $\omega_{xs} = (\omega_{10}, \omega_{20})$ respectively, because the effective energy windows become narrower than the X-ray probe bandwidth. For $\sigma = 30$ eV$^{-1/2}$ and $\lambda = 5.2$, the two are almost completely separated.

Figure 6 shows the diffraction signals given by eqs 3, 8, and 12 for scattering off the $|e\rangle\langle e|$ population for different frequencies ω_{xs}. Diagrams c (elastic when $e_1 = e_2 = e_3$; inelastic when $e_1 = e_3 \neq e_2$) and d (inelastic (anti-Stokes) when $e_1 = e_2$) can contribute to the signal as shown in the figure. These signals are time-independent, because the electronic density matrix element ρ_{ee} does not vary with time. The signals are proportional to the modulus square of the corresponding transition charge density diagram c, elastic: $S \propto \rho_{ee}|\sigma_{ee}|^2$, diagram c, inelastic: $S \propto \rho_{ee}|\sigma_{ee}|^2$, or diagram d, inelastic (Anti-Stokes): $S \propto \rho_{ee}|\sigma_{ge}|^2$. The signals depend on the initially prepared population ρ_{ee}. One can resolve the Stokes, the elastic, and the anti-Stokes contributions by tuning ω_{xs} to be positive, zero, and negative in resonance with the Raman shift of a target diffraction, respectively.

DOI: 10.1021/acs.jpclett.9b00924
J. Phys. Chem. Lett. 2019, 10, 5805−5814

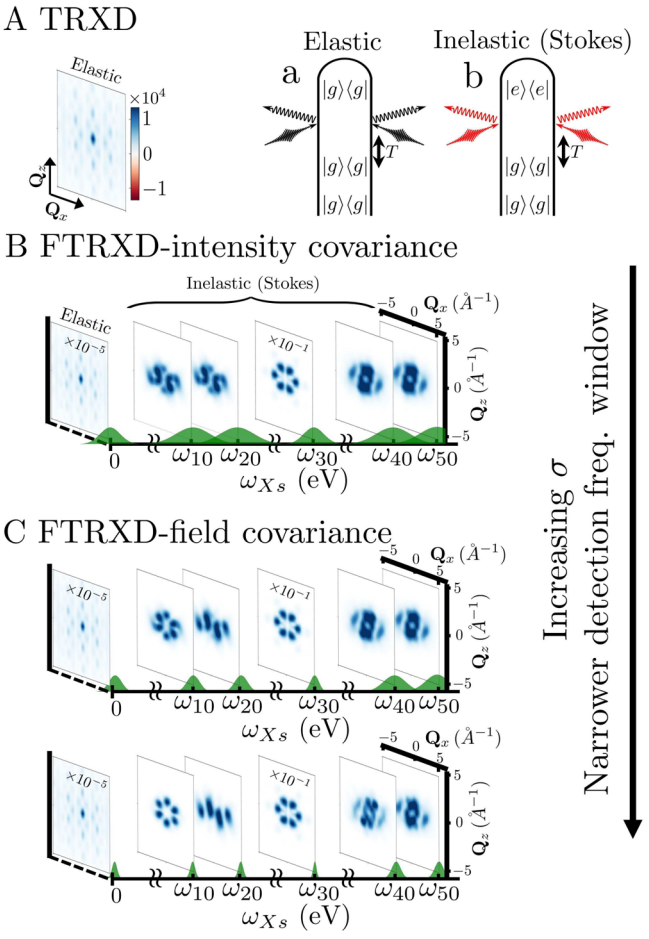

Figure 5. Scattering off the ground-state $|g\rangle\langle g|$ population. The signals are independent of the time-delay T. (A) Noise free ($\sigma = 0$) incoherent time-resolved X-ray diffraction (TRXD) signals (eq 3). Loop diagrams describing the process are shown (to the right). (B) Frequency-resolved incoherent diffraction signals from signal-intensity cross correlation $C_{SI}(\bar{\omega}_s, \omega_p, \mathbf{Q}, T)$ (eq 8) as a function of ω_{xs}, Demonstrating that the elastic or inelastic scatterings can be resolved separately by scanning the Raman frequency ω_{xs}. The joint noise-gating effective frequency windows are schematically shown as green Gaussian envelopes. (C) Frequency-resolved incoherent diffraction signals from diffraction-field cross correlation $C_{S;EE}(\omega_s, \omega_1, \omega_2, \mathbf{Q}, T)$ (eq 12) as a function of ω_{xs} for different degrees of stochasticity (σ). As σ increases from (top) 15 to (bottom) 30, the effective energy window of the frequency-gating (green Gaussian envelopes) becomes narrower as $\propto 1/\lambda^2\sigma^2$ compared to $C_{SI}(\bar{\omega}_s, \omega_p, \mathbf{Q}, T)$ ([shown in panel B) which results in sharper separation between the processes. When $\sigma = 0$, eq 12 corresponds to eq 8. The real part of the signal is presented in all panels.

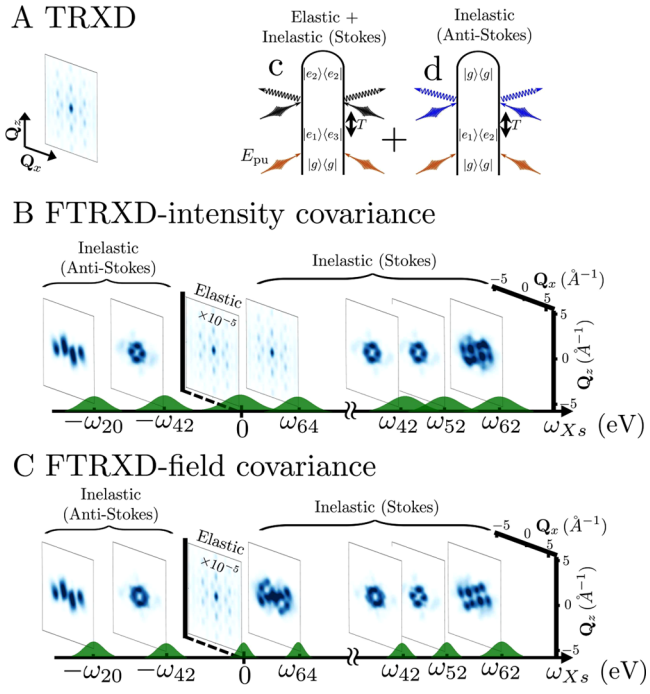

Figure 6. Similar to Figure 5, presenting the scattering off the excited-state population $|e\rangle\langle e|$ with increasing noise power.

Ordinary TRXD (Figure 6A) is dominated by the elastic contribution because the diagonal charge density is much larger than the off-diagonal ($\sigma_{ge} \ll \sigma_{ee}$). It is thus not possible to retrieve the inelastic contributions.

The FTRXD-intensity correlation shown in Figure 6 can resolve the Stokes from the elastic by scanning the Raman frequency ω_{xs} on resonance with a transition frequency of $\omega_{e'e}$. The middle panel of Figure 6 singles out the elastic contribution by scattering off the excited-state charge density σ_{ee} when $\omega_{xs} = 0$. In the right panels, the Stokes processes corresponding to the $|e\rangle\langle e| \rightarrow |e'\rangle\langle e'|$ transitions can be resolved by tuning $\omega_{xs} = \omega_{e'e} > 0$. The signals are then $S \propto \rho_{ee}|\sigma_{e'e}|^2$. Conversely, by setting $\omega_{xs} = -\omega_{ee'} < 0$ (when $e > e'$) the anti-Stokes contribution of the transition $|e\rangle\langle e| \rightarrow |e'\rangle\langle e'|$ is selected. However, the processes with close Raman shifts, for example, $\omega_{xs} = (0,\omega_{64})$ and $(\omega_{42},\omega_{52})$, are not resolved. The signals for low Raman frequencies such as $\omega_{xs} = \omega_{64}$ are covered by the much stronger elastic contributions at $\omega_{xs} = 0$.

Figure 6 demonstrate the high performance of multidimensional signal−field cross-correlations for providing an enhanced frequency resolution. Figure 6 uses a noise fluctuation standard deviation ($\sigma = 30$) in eq 12 by tuning $\omega_{xs} = \omega_{e'e}$, $\omega_{1s} = \omega_{2s} = \omega_{ee'}$. It is evident that the frequency resolution is enhanced by increasing σ and the diffraction processes at $\omega_{xs} = (0, \omega_{64})$ and $(\omega_{42}, \omega_{52})$ are clearly resolved.

Figure 7 shows the diffraction signals (eqs 3, 8, and 12), describing scattering from the coherences $|g\rangle\langle e|$ and resolved by varying ω_{xs}. Two contributions arise from the $|g\rangle\langle e|$, which ends in the ground population $|g\rangle\langle g|$ and the excited state population $|e'\rangle\langle e'|$. These signals are time-dependent, and the dynamics results from $\rho_{ge}(T) = \rho_{ge}(0)e^{-i\omega_{ge}T}$. The signals are proportional to the product of two transition charge densities $S \propto \rho_{ge}\sigma_{gg}\sigma^*_{e_1g}$ or $S \propto \rho_{ge}\sigma_{ge_2}\sigma^*_{e_1e_2}$ for E and F, respectively. Complex conjugates of these contributions H and G also contribute to the signal from the $|e\rangle\langle g|$ coherence. We note that diagrams e and f when $e_1 = e_2$ dominate the signal with comparable amplitudes while the contribution from diagram f when $e_1 \neq e_2$ is 10^{-3} times weaker.

Figure 7 (left panel) depicts the diffraction pattern from all possible Raman processes for scattering off $|g\rangle\langle e|$ coherences. It is not possible to extract a single component out of the total signal. From the Fourier transform of the time-domain signal intensity at point 1, the coordinate in the $\mathbf{Q}$-space $(\mathbf{Q}_x, \mathbf{Q}_y) = (-1.44\ \text{Å}^{-1}, 0.00\ \text{Å}^{-1})$, scattering off the $|0\rangle\langle 2|$, $|0\rangle\langle 4|$, and $|$

DOI: 10.1021/acs.jpclett.9b00924
J. Phys. Chem. Lett. 2019, 10, 5805−5814

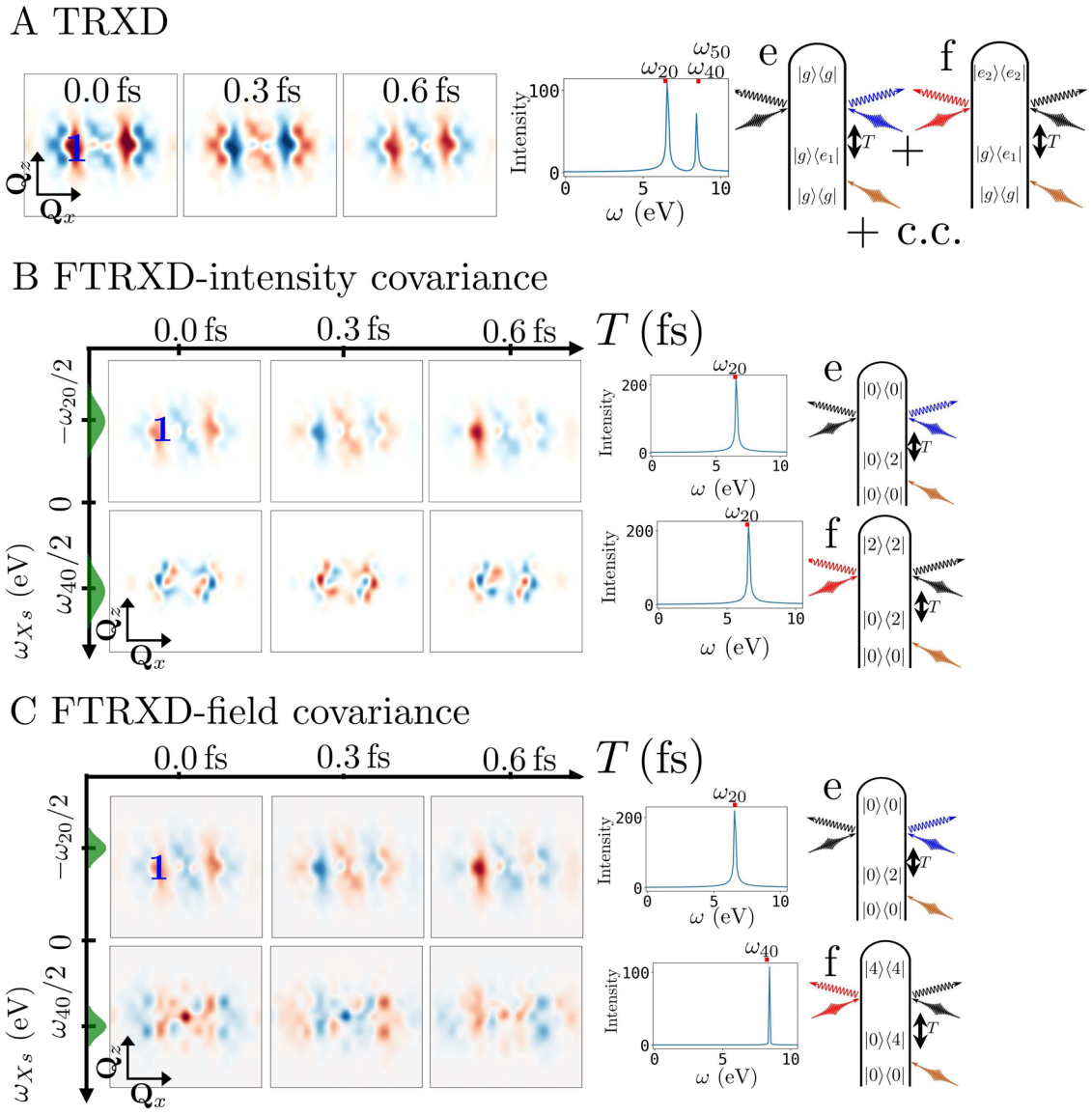

Figure 7. Scattering off the $|g\rangle\langle e|$ coherence. The temporal evolution is given by an oscillation at frequency ω_{ge}. (A) Noise-free ($\sigma = 0$) incoherent time-resolved X-ray diffraction (TRXD) is shown (eq 3. The diagrams describing the process are presented (to the right). (B) Left: Frequency-resolved incoherent diffraction signals from signal-intensity cross correlation $C_{SI}(\bar{\omega}_s, \omega_p, \mathbf{Q}, T)$ (eq 8) as a function of ω_{xs}. The effective frequency-gating windows are schematically depicted as green envelopes from the left. Middle: Fourier transformation of the evolution of the signal at 1 [$(\mathbf{Q}_x, \mathbf{Q}_z) = (-1.44\ \text{Å}^{-1}, 0\ \text{Å}^{-1})$]. Right: Corresponding loop diagrams. (C) Frequency-resolved incoherent diffraction signals from diffraction-field cross correlations $C_{S;EE}(\omega_s, \omega_1, \omega_2, \mathbf{Q}, T)$ (eq 12) as a function of ω_{xs} for ($\sigma = 30$). By tuning $\omega_{1s} = \omega_{ab}$ and $\omega_{2s} = \omega_{cb}$ (see Figure 1a for a, b, and c notation), a diffraction process represented by a single loop diagram was singled out. The real part of the signal is presented in all panels.

$0\rangle\langle 5|$ coherences contributes to the total signal (Figure 7A middle panel).

Figure 7 presents the FTRXD-intensity correlation, where the transition in diagram e is resolved ($|g\rangle\langle e| \rightarrow |g\rangle\langle g|$) by tuning $\omega_{xs} = -\omega_{eg}/2 < 0$. Similarly, the process shown in diagram f ($|g\rangle\langle e_1| \rightarrow |e_2\rangle\langle e_2|$) is resolved by tuning $\omega_{xs} = (\omega_{e_2 g} + \omega_{e_2 e_1})/2$. For $\omega_{xs} = -\omega_{20}/2$, the signal stemming from scattering off the $|0\rangle\langle 2| \rightarrow |0\rangle\langle 0|$ was resolved (Figure 7B, top left panels). This is confirmed by the Fourier transform of the signal intensity in the time domain at 1, showing the signal at ω_{20} which is a manifestation of $|0\rangle\langle 2|$ coherence. However, a resolution of the diffraction process $|0\rangle\langle 4| \rightarrow |4\rangle\langle 4|$ is not successful even though we tune $\omega_{xs} = -\omega_{40}/2$. The signal at ω_{40} expected to be observed by the $|0\rangle\langle 4|$ coherence is not observed in the Fourier transform, rather we observe ω_{20} given by the $|0\rangle\langle 2|$ coherence in Figure 7 (bottom middle panel). This is because the effective frequency-gating for the process $\overline{\mathbf{A}^s_{44}\mathbf{A}^{s*}_{04}}$ is much smaller than the others. When the transition frequency difference on the two branches of the loop is large ($\omega_{ab} - \omega_{cb}$, see Figure 1A for the labeling), keeping both frequency gatings in the diffraction probe bandwidth is difficult.

To resolve this issue, we next demonstrate that the FTXRD-field cross-correlations provide an enhanced frequency resolution, by tuning ω_{1s} and ω_{2s} in resonance with the transition frequency on the left and right branches of the loop diagram, respectively. Figure 7 bottom shows a calculation using a noise fluctuation standard deviation ($\sigma = 30$) in eq 12 by tuning $\omega_{xs} = \omega_{40}/2$, $\omega_{1s} = \omega_{04}$, and $\omega_{2s} = 0$. It is evident that

DOI: 10.1021/acs.jpclett.9b00924
J. Phys. Chem. Lett. 2019, 10, 5805−5814

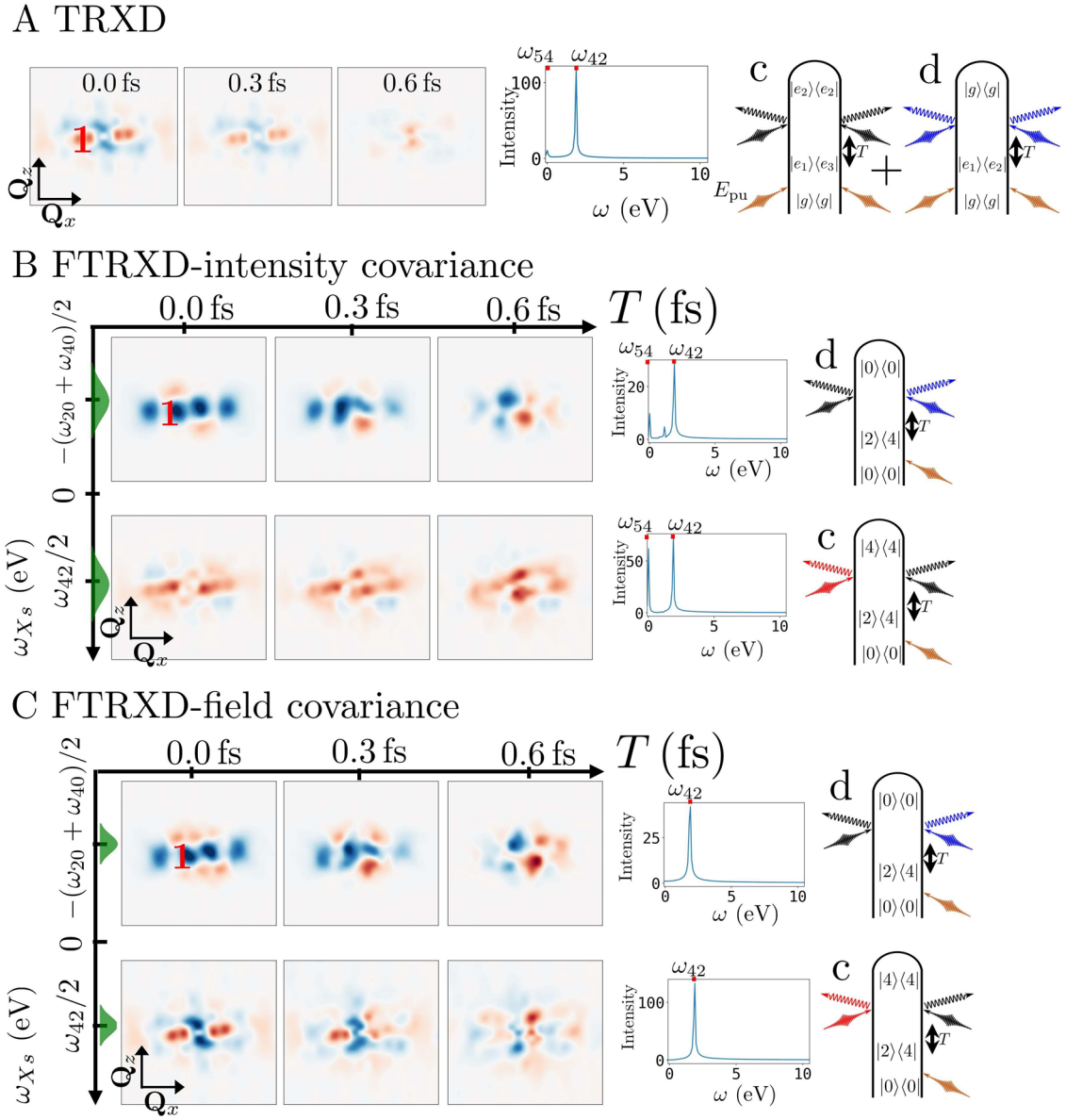

Figure 8. Equivalent to Figure 7, considering the scattering off the $|e\rangle\langle e'|$ coherence with increasing noise power.

the signal stems from the $|0\rangle\langle 4|$ coherence from the Fourier transform of the time-domain response at 1.

Figure 8 displays the diffraction signals (eqs 3, 8, and 12) for scattering off the $|e\rangle\langle e'|$ coherence for different frequencies ω_{xs}. The two contributions arising from $|e\rangle\langle e'|$ are shown in the figure (diagram c when $e_1 \neq e_3$ and diagram d when $e_1 \neq e_2$). These signals are time-dependent through $\rho_{ee'}(T) = \rho_{ee'}(0)e^{-i\omega_{ee'}T}$. The signals are proportional to the product of the two transition charge densities $S \propto \rho_{ee'}\sigma_{e_1e_2}\sigma^*_{e_3e_2}$ or $S \propto \rho_{ee'}\sigma_{e_1g}\sigma^*_{e_2g}$ for diagrams c and d, respectively.

The TRXD signal depicted in Figure 8 is a result of many possible Raman processes from all $|e\rangle\langle e'|$ excited coherences. The dominant $|e\rangle\langle e'|$ coherences can be identified by the Fourier transform of the time-domain signal intensity at point 1 (Q_x, Q_y) = (−1.44 Å^{-1}, 0.00 Å^{-1}). It is evident that the scattering off the $|2\rangle\langle 4|$ and $|4\rangle\langle 5|$ coherences contributes largely to the total signal (Figure 8A, middle panel). However, it is not possible to single out a single component out of the total signal, in the ordinary TRXD.

> The apparent shortcomings of stochastic X-ray sources can be turned into a useful tool, providing a novel continuous experimental knob that controls the joint time−frequency resolutions.

The FTRXD-intensity correlation (Figure 8B) can resolve the process displayed in diagram c ($|e_1\rangle\langle e_3| \rightarrow |e_2\rangle\langle e_2|$) by tuning $\omega_{xs} = (\omega_{e_2e_1} + \omega_{e_2e_3})/2$ and diagram d ($|e_1\rangle\langle e_2| \rightarrow |g\rangle\langle g|$) by tuning $\omega_{xs} = -(\omega_{e_1g} + \omega_{e_2g})/2 < 0$. Setting $\omega_{xs} = -(\omega_{20} + \omega_{40})/2$, one can attempt to resolve the $|2\rangle\langle 4| \rightarrow |0\rangle\langle 0|$ transition. However, as shown in the Fourier transform of the signal at 1 in the time-domain, a single transition process is not

DOI: 10.1021/acs.jpclett.9b00924
J. Phys. Chem. Lett. 2019, 10, 5805−5814

resolved, because the Raman frequencies of other diffraction processes may fall into a similar energy range of the target diffraction process $|2\rangle\langle 4| \rightarrow |0\rangle\langle 0|$. Therefore, the total signals contain a mixture of various diffraction processes.

We now demonstrate how the FTXRD-field correlation technique enhances the frequency resolution and resolves this issue. In addition to tuning $\omega_{xs} = -(\omega_{20}+\omega_{40})/2$, we can single out the $|2\rangle\langle 4| \rightarrow |0\rangle\langle 0|$ transition by tuning $\omega_{1s} = \omega_{20}$ and $\omega_{2s} = \omega_{40}$ as shown in Figure 8, top left. It is evident that the signal stems from the $|2\rangle\langle 4|$ coherence from the Fourier transformation of the time-domain response at 1. Similarly, by tuning $\omega_{xs} = -\omega_{42}/2$, one can single out the $|2\rangle\langle 4| \rightarrow |4\rangle\langle 4|$ transition by tuning $\omega_{1s} = \omega_{24}$ and $\omega_{2s} = 0$.

We have demonstrated how the apparent shortcomings of stochastic X-ray sources with random phase can be turned into a useful tool, providing a novel continuous experimental knob that controls the joint time−frequency resolutions. The molecular evolution is monitored by varying the delay between the two pulses. The stochastic phase components which mark each frequency uniquely, permit a higher spectral resolution, but reduce the temporal resolution by blurring the interaction time with the probe pulse. Our approach continuously follows the transition from multiplicative to additive noise as the stochasticity parameter λ is small, allowing pertubative expansion that results in amplitude fluctuations.

Diffraction of a bright source by matter is a second-order process involving two charge-density factors. The signal averaged over stochastic realizations is expressed in terms of two-point correlation functions of the field. Higher-order correlation functions provide a rich multidimensional variable space that can be optimized by postprocessing protocols to identify and distinguish between different contributions to the diffraction pattern. The stochastic phase distribution is expressed in the averaged signal as the characteristic function of the noise distribution. Noise shaping techniques can thus be used to control spectro-temporal properties of the optical window, considering that the relation between the noise distribution and its characteristic function is given by a Fourier transform. For example, a normalized time sinc distribution will result in a rectangular spectral characteristic function with a flat center and sharply decaying boundaries. This is very useful as a frequency window, capturing the dynamics with minimal distortion. Such techniques offer extraordinary working tools in the study of complex-multiscale systems and require further study.

■ ASSOCIATED CONTENT

Supporting Information

The Supporting Information is available free of charge on the ACS Publications website at DOI: 10.1021/acs.jpclett.9b00924.

X-ray diffraction signal (Appendix A) and construction of multidimensional stochastic resonance diffraction signals (Appendix B) (PDF)

■ AUTHOR INFORMATION

Corresponding Authors

*E-mail: Shahaf.S.Asban@gmail.com.
*E-mail: daeheumc@uci.edu.
*E-mail: smukamel@uci.edu.

ORCID

Daeheum Cho: 0000-0002-0322-4291

Shaul Mukamel: 0000-0002-6015-3135

Author Contributions

‡S.A. and D.C. contributed equally.

Notes

The authors declare no competing financial interest.

■ ACKNOWLEDGMENTS

We gratefully acknowledge the support of the National Science Foundation (Grant CHE-1663822) (S.A.) and the Chemical Sciences, Geosciences, and Biosciences division, Office of Basic Energy Sciences, Office of Science, U.S. Department of Energy through award DE-FG02-04ER15571 (D.C.).

■ REFERENCES

(1) Weninger, C.; Purvis, M.; Ryan, D.; London, R. A.; Bozek, J. D.; Bostedt, C.; Graf, A.; Brown, G.; Rocca, J. J.; Rohringer, N. Stimulated Electronic X-Ray Raman Scattering. *Phys. Rev. Lett.* **2013**, *111*, 233902.

(2) Weninger, C.; Rohringer, N. Stimulated resonant x-ray Raman scattering with incoherent radiation. *Phys. Rev. A: At., Mol., Opt. Phys.* **2013**, *88*, 053421.

(3) Tollerud, J. O.; Sparapassi, G.; Montanaro, A.; Asban, S.; Glerean, F.; Giusti, F.; Marciniak, A.; Kourousias, G.; Billè, F.; Cilento, F.; Mukamel, S.; Fausti, D. Femtosecond covariance spectroscopy. *Proc. Natl. Acad. Sci. U. S. A.* **2019**, *116*, 5383−5386.

(4) Ishikawa, T.; et al. A compact X-ray free-electron laser emitting in the sub-ångström region. *Nat. Photonics* **2012**, *6*, 540.

(5) Emma, P.; et al. First lasing and operation of an ångstrom-wavelength free-electron laser. *Nat. Photonics* **2010**, *4*, 641.

(6) Allaria, E.; et al. Two-stage seeded soft-X-ray free-electron laser. *Nat. Photonics* **2013**, *7*, 913.

(7) Gorobtsov, O. Y.; Mercurio, G.; Brenner, G.; Lorenz, U.; Gerasimova, N.; Kurta, R. P.; Hieke, F.; Skopintsev, P.; Zaluzhnyy, I.; Lazarev, S.; Dzhigaev, D.; Rose, M.; Singer, A.; Wurth, W.; Vartanyants, I. A. Statistical properties of a free-electron laser revealed by Hanbury Brown−Twiss interferometry. *Phys. Rev. A: At., Mol., Opt. Phys.* **2017**, *95*, 023843.

(8) Singer, A.; et al. Spatial and temporal coherence properties of single free-electron laser pulses. *Opt. Express* **2012**, *20*, 17480−17495.

(9) Vartanyants, I. A.; et al. Coherence Properties of Individual Femtosecond Pulses of an X-Ray Free-Electron Laser. *Phys. Rev. Lett.* **2011**, *107*, 144801.

(10) Gorobtsov, O. Y.; et al. Diffraction based Hanbury Brown and Twiss interferometry at a hard x-ray free-electron laser. *Sci. Rep.* **2018**, *8*, 2219.

(11) Gauthier, D.; Ribic, P. R.; De Ninno, G.; Allaria, E.; Cinquegrana, P.; Danailov, M. B.; Demidovich, A.; Ferrari, E.; Giannessi, L.; Mahieu, B.; Penco, G. Spectrotemporal Shaping of Seeded Free-Electron Laser Pulses. *Phys. Rev. Lett.* **2015**, *115*, 114801.

(12) Gammaitoni, L.; Hänggi, P.; Jung, P.; Marchesoni, F. Stochastic resonance. *Rev. Mod. Phys.* **1998**, *70*, 223−287.

(13) Morita, N.; Yajima, T. Ultrahigh-time-resolution coherent transient spectroscopy with incoherent light. *Phys. Rev. A: At., Mol., Opt. Phys.* **1984**, *30*, 2525−2536.

(14) Asaka, S.; Nakatsuka, H.; Fujiwara, M.; Matsuoka, M. Accumulated photon echoes with incoherent light in Nd^{3+}-doped silicate glass. *Phys. Rev. A: At., Mol., Opt. Phys.* **1984**, *29*, 2286−2289.

(15) Beach, R.; Hartmann, S. R. Incoherent Photon Echoes. *Phys. Rev. Lett.* **1984**, *53*, 663−666.

(16) Kobayashi, T.; Terasaki, A.; Hattori, T.; Kurokawa, K. The application of incoherent light for the study of femtosecond-picosecond relaxation in condensed phase. *Appl. Phys. B: Photophys. Laser Chem.* **1988**, *47*, 107−125.

(17) Mukamel, S. *Principles of nonlinear optical spectroscopy*; Oxford series in optical and imaging sciences; Oxford University Press, 1995.

(18) Kimberg, V.; Rohringer, N. Stochastic stimulated electronic x-ray Raman spectroscopy. *Struct. Dyn.* **2016**, *3*, 034101.

DOI: 10.1021/acs.jpclett.9b00924
J. Phys. Chem. Lett. 2019, 10, 5805−5814

(19) Bennett, K.; Biggs, J. D.; Zhang, Y.; Dorfman, K. E.; Mukamel, S. Time-, frequency-, and wavevector-resolved x-ray diffraction from single molecules. *J. Chem. Phys.* **2014**, *140*, 204311.
(20) Bennett, K.; Kowalewski, M.; Rouxel, J. R.; Mukamel, S. Monitoring molecular nonadiabatic dynamics with femtosecond X-ray diffraction. *Proc. Natl. Acad. Sci. U. S. A.* **2018**, *115*, 6538−6547.

DOI: 10.1021/acs.jpclett.9b00924
J. Phys. Chem. Lett. 2019, 10, 5805−5814

Appendices for "Frequency-resolved ultrafast single-molecule diffraction of noisy X-ray pulses"

Shahaf Asban, Daeheum Cho, and Shaul Mukamel
Department of Chemistry and Physics and Astronomy, University of California, Irvine, California 92697-2025, USA

Appendix A: The X-ray diffraction signal

The signal is given by the intensity of the diffracted field,

$$S\left(\omega_s, t_s, \boldsymbol{k}_s, \boldsymbol{r}_s\right) = \int d\boldsymbol{r}dt, \left\langle \boldsymbol{E}^{\dagger(t\boldsymbol{r}f\boldsymbol{k})}\left(\boldsymbol{r},t\right)\boldsymbol{E}^{(t\boldsymbol{r}f\boldsymbol{k})}\left(\boldsymbol{r},t\right)e^{-\frac{i}{\hbar}\int_{-\infty}^{t}d\tau\mathcal{H}_{I-}(\tau)}\right\rangle, \tag{A1}$$

where ω_s is the measured frequency, t_s is the measurement time, $\boldsymbol{k}_s$ is the wavevector and $\boldsymbol{r}_s$ is the measurement location. The field is given by,

$$\boldsymbol{E}\left(\boldsymbol{r},t\right) = \frac{1}{\left(2\pi\right)^4}\int d\omega \int d^3\boldsymbol{k}\boldsymbol{E}\left(\boldsymbol{k},\omega\right)e^{i\boldsymbol{k}\cdot\boldsymbol{r}-i\omega_{\boldsymbol{k}}t}. \tag{A2}$$

The electric field is subjected to a spectro-temporal gating using the following procedure Bennett *et al.* [1],

$$\begin{aligned}
\boldsymbol{E}^{(t)}\left(\boldsymbol{r},t\right) &= F_t\left(t,\bar{t}\right)\boldsymbol{E}\left(\boldsymbol{r},t\right), \\
\boldsymbol{E}^{(t\boldsymbol{r})}\left(\boldsymbol{r},t\right) &= F_{\boldsymbol{r}}\left(\boldsymbol{r},\bar{\boldsymbol{r}}\right)\boldsymbol{E}^{(t)}\left(\boldsymbol{r},t\right), \\
\boldsymbol{E}^{(t\boldsymbol{r}f)}\left(\boldsymbol{r},t\right) &= F_f\left(\omega,\bar{\omega}\right)\boldsymbol{E}^{(t\boldsymbol{r})}\left(\boldsymbol{r},\omega\right), \\
\boldsymbol{E}^{(t\boldsymbol{r}f\boldsymbol{k})}\left(\boldsymbol{r},t\right) &= F_{\boldsymbol{k}}\left(\boldsymbol{k},\bar{\boldsymbol{k}}\right)\boldsymbol{E}^{(t\boldsymbol{r}f)}\left(\boldsymbol{k},\omega\right),
\end{aligned} \tag{A3}$$

where $F_X\left(X,\bar{X}\right)$ is a gating function from the physical coordinate X to the measured one $\bar{X}$. The signal can be recast in the form,

$$S\left(\omega_s,t_s,\boldsymbol{k}_s,\boldsymbol{r}_s\right) = \int\frac{d\omega}{2\pi}dt\int\frac{d\boldsymbol{k}}{\left(2\pi\right)^3}d\boldsymbol{r}W_B\left(t,\omega,\boldsymbol{r},\boldsymbol{k}\right)W_D\left(t,\omega,\boldsymbol{r},\boldsymbol{k};t_s,\omega_s,\boldsymbol{r}_s,\boldsymbol{k}_s\right), \tag{A4}$$

where,

$$W_D\left(t,\omega,\boldsymbol{r},\boldsymbol{k};t_s,\omega_s,\boldsymbol{r}_s,\boldsymbol{k}_s\right) = \int\frac{d\omega}{2\pi}\left|F_f\left(\omega,\omega_s\right)\right|^2 W_t\left(t,t_s,\omega-\omega_s\right)\int\frac{d^3\boldsymbol{k}}{\left(2\pi\right)^3}\left|F_{\boldsymbol{k}}\left(\boldsymbol{k},\boldsymbol{k}_s\right)\right|^2 W_{\boldsymbol{r}}\left(\boldsymbol{r},\boldsymbol{r}_s,\boldsymbol{k}-\boldsymbol{k}_s\right), \tag{A5}$$

is the detector spectogram and,

$$W_B\left(t,\omega,\boldsymbol{r},\boldsymbol{k}\right) = \int d\tau e^{-i\omega\tau}\int d\boldsymbol{R}e^{i\boldsymbol{k}\cdot\boldsymbol{R}}\left\langle\mathcal{T}\boldsymbol{E}_R^{\dagger}\left(\boldsymbol{r}+\frac{\boldsymbol{R}}{2},t+\frac{\tau}{2}\right)\boldsymbol{E}_L\left(\boldsymbol{r}-\frac{\boldsymbol{R}}{2},t-\frac{\tau}{2}\right)\right\rangle. \tag{A6}$$

is the bare signal spectogram is. The modes initially in the vacuum state are given by the vector potential,

$$\boldsymbol{A}\left(\boldsymbol{r},t\right) = \sum_{\boldsymbol{k},\mu}\sqrt{\frac{2\pi\hbar}{V\omega_{\boldsymbol{k}}}}\epsilon^{(\mu)}\left(\boldsymbol{k}\right)a_{\boldsymbol{k},\mu}e^{i\boldsymbol{k}\cdot\boldsymbol{r}-i\omega_{\boldsymbol{k}}t}, \tag{A7}$$

and,

$$\boldsymbol{A}_p\left(\boldsymbol{r},t\right) = \bar{\epsilon}\left(\boldsymbol{k}_p\right)\int\frac{d\omega}{2\pi}A_p\left(\omega\right)e^{i\boldsymbol{k}_p\cdot\boldsymbol{r}-i\omega t}, \tag{A8}$$

where $\bar{\epsilon}\left(\boldsymbol{k}_p\right)$ is the average polarization of the classical probe field .

The off-resonant resonant scattering of light by matter is described by the the minimal coupling,

$$\mathcal{H}_I = \int d\boldsymbol{r}\hat{\sigma}\left(\boldsymbol{r},t\right)\hat{\boldsymbol{A}}^2\left(\boldsymbol{r},t\right), \tag{A9}$$

where $\hat{\sigma}$ is the charge density operator and $\boldsymbol{A}$ is the vector potential. When the probe field is taken to classical, the first nonvanishing contribution to Eq.(A1) requires two interactions as depicted diagrammatically in Fig.(1). Solving Eq.(A4) using an ideal spatial gating,

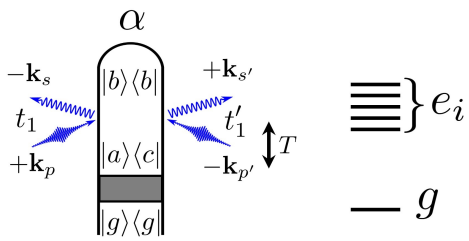

Figure 1. Diagrammatic description of off-resonant diffraction.

$$W_D\left(\boldsymbol{r},\boldsymbol{r}_s,\boldsymbol{k},\boldsymbol{k}_s\right)=\delta^{(3)}\left(\boldsymbol{r}-\boldsymbol{r}_s\right), \tag{A10}$$

as done in Bennett *et al.* [1], we obtain Eq.(3) of the main text,

$$\begin{aligned} S^{[1]}\left(\bar{\omega}_s,\boldsymbol{Q},T;\Lambda\right)=NK\int d\omega_s\,\omega_s^2 G\left(\omega_s,\bar{\omega}_s\right)\omega_s^2\sum_{abc}\rho_{ac}\left(T\right) \\ \times\sigma_{ba}\left[\boldsymbol{Q}\left(\omega_s\right)\right]\sigma_{bc}^*\left[\boldsymbol{Q}\left(\omega_s\right)\right]\left\langle \boldsymbol{A}_p\left(\omega_s+\omega_{ba}\right)\boldsymbol{A}_p^*\left(\omega_s+\omega_{bc}\right)\right\rangle_\Lambda . \end{aligned} \tag{A11}$$

where N is the number of particles and,

$$K=\frac{\left|\hat{\epsilon}\left(\boldsymbol{k}_p\right)\cdot\epsilon_s^*\right|^2}{72\pi r^2c^4}. \tag{A12}$$

Appendix B: Construction of multidimensional stochastic resonance diffraction signals

1. Second order stochastic resonance: Signal-Intensity covariance

We consider a higher order post-processing calculation than mean signal by measuring the time-resolved intensity of the incident field. Once the intensity is measured Vs. time, its Fourier transform carries the phase fluctuations information of each experimental realization. The frequency domain intensity is given by,

$$\begin{aligned} I(\omega_p) &= \int dt e^{-i\omega_p t} \left|\boldsymbol{E}_p(t)\right|^2 \\ &= 2\pi \int d\omega' \omega' \left(\omega' + \omega_p\right) A^*\left(\omega'\right) A\left(\omega' + \omega_p\right) e^{-i\lambda\left\{\varphi\left[\omega'\right] - \varphi\left[\omega' + \omega_p\right]\right\}}. \end{aligned} \tag{B1}$$

The cross-correlation of the diffraction signal with a given frequency of the intensity,

$$\begin{aligned} \mathcal{S}_{SI}(\omega_s, \omega_p, \boldsymbol{Q}, T) &= \left\langle I[\omega_p; \Lambda] S^{[1]}(\omega_s, \boldsymbol{Q}, T; \Lambda) \right\rangle_\Lambda / 2\pi\kappa_1 \\ &= \sum_{abc} \sigma_{ba}(\boldsymbol{Q}) \sigma_{bc}^*(\boldsymbol{Q}) \boldsymbol{A}_{ab}^s \boldsymbol{A}_{cb}^{s*} e^{i\omega_{ca} T} \\ &\times \int d\omega E(\omega) E^*(\omega + \omega_p) \\ &\left\langle e^{i\lambda\left\{\varphi_{ab}^s - \varphi_{cd}^s - \varphi[\omega] + \varphi[\omega + \omega_p]\right\}} \right\rangle, \end{aligned} \tag{B2}$$

the contribution of the last two terms comes from two separate intervals. The first when $(\omega, \omega + \omega_p)$ does not overlap with $(\omega_s + \omega_{ab}, \omega_s + \omega_{cb})$ is denoted Ω_{ind}, and second when they do will be denoted Ω_{corr},

$$\begin{aligned} \int d\omega E(\omega) E^*(\omega + \omega_p) \left\langle e^{i\lambda\{\varphi_{ab}^s - \varphi_{cd}^s - \varphi[\omega] + \varphi[\omega + \omega_p]\}} \right\rangle &= e^{-\lambda^2\sigma^2[|\omega_p| + |\omega_{ac}|]} I[\Omega_{ind}] \\ &+ \int_{\Omega_{corr}} d\omega E(\omega) E^*(\omega + \omega_p) e^{-\lambda^2\sigma^2[|\omega_s + \omega_{ab} - \omega| + |\omega_s + \omega_{cb} - \omega_p - \omega|]}, \end{aligned} \tag{B3}$$

where $I[\Omega_{ind}] = \int_{\Omega_{ind}} d\omega E(\omega) E^*(\omega + \omega_p)$. The average intensity is given by,

$$\langle I[\omega_p; \Lambda] \rangle_\Lambda = I_p e^{-\lambda^2\sigma^2|\omega_p|}, \tag{B4}$$

where I_p is the frequency-integrated intensity. This leads to a difference between the average intensity and the one correlated with the diffraction signal. In order to concentrate on the phase mixing terms which result in a higher temporal resolution, we assume that the interval $(\omega_s + \omega_{ab}, \omega_s + \omega_{cb})$ only contributes marginally to I_p such that the covariance $\mathcal{C}_{SI}$ reads,

$$\begin{aligned} \mathcal{C}_{SI}(\omega_s, \omega_p, \boldsymbol{Q}, T) &= \left[\left\langle I[\omega_p; \Lambda] S^{[1]}(\omega_s, \boldsymbol{Q}, T; \Lambda) \right\rangle_\Lambda - \langle I[\omega_p; \Lambda] \rangle_\Lambda \left\langle S^{[1]}(\omega_s, \boldsymbol{Q}, T; \Lambda) \right\rangle_\lambda \right] / 2\pi\kappa_1 \\ &= \sum_{abc} \sigma_{ba}(\boldsymbol{Q}) \sigma_{bc}^*(\boldsymbol{Q}) \boldsymbol{A}_{ab}^s \boldsymbol{A}_{cb}^{s*} e^{i\omega_{ca} T} \\ &\times \left[\int_{\Omega_{corr}} d\omega E(\omega) E^*(\omega + \omega_p) \right. \\ &\left. \times e^{-\lambda^2\sigma^2\left[|\omega_s + \omega_{ab} - \omega| + \left|\omega_s + \omega_{cb} - \omega_p - \omega\right|\right]} + \delta I_p[\Omega_{corr}] \right], \end{aligned} \tag{B5}$$

where,

$$\delta I_p = I[\Omega_{ind}] e^{-\lambda^2\sigma^2[|\omega_p| + |\omega_{ac}|]} - I_p e^{-\lambda^2\sigma^2|\omega_p|}. \tag{B6}$$

when the interval $(\omega_s+\omega_{ab}\pm\omega_p,\omega_s+\omega_{cb}\pm\omega_p)$ does not include the central frequency and $\lambda\sigma$ is large, δI_p becomes negligible which results in the phase-mixing terms only. When the phase fluctuations are strong and σ is larger than the pulse bandwidth such that the exponent in Eq.$(B5)$ is rapidly decreasing and the field envelope can be considered to be constant throughout the integration interval of Ω_{corr}, we can estimate the integral,

$$\begin{aligned}&\int d\omega E\left(\omega+\omega_s+\omega_{ab}\right)\\&\times E^*\left(\omega+\omega_p+\omega_s+\omega_{ab}\right)e^{-\lambda^2\sigma^2|\omega-\Delta|}\\&\approx I_p\left[\Omega_{corr}\right]\frac{2}{\lambda^2\sigma^2},\end{aligned}\tag{B7}$$

where $\Delta=\omega_{ca}-\omega_p$. This constant sum in contrast to $\mathcal{S}_{SI}$, where averaging over many realizations with fluctuating phase results in a trade-off between frequency and temporal resolution. The signal in this case reads,

$$\begin{aligned}\mathcal{C}_{SI}\left(\omega_s,\omega_p,\boldsymbol{Q},T\right)&=\kappa_2^{-1}\mathcal{C}ov_\Lambda\left\{I\left[\omega_p;\Lambda\right]S^{[1]}\left(\omega_s,\boldsymbol{Q},T;\Lambda\right)\right\}\\&=\sum_{abc}\sigma_{ba}\left(\boldsymbol{Q}\right)\sigma_{bc}^*\left(\boldsymbol{Q}\right)\overline{\boldsymbol{A}_{ab}^s\boldsymbol{A}_{cb}^{s*}}e^{i\omega_{ca}T},\end{aligned}\tag{B8}$$

and $\kappa_2^{-1}=\frac{\pi\kappa_1}{\sigma^2\lambda^2}I_p\left[\Omega_{corr}\right]$. This signal recovers the single molecule diffraction studied in [2] and contains the full temporal dynamics.

2. Diffraction-Field covariance

We now imagine a scenario in which the frequency dispersed expression for the electric field (including the phase) can be stored for each realization of the stochastic field. This is possible by heterodyne measurement of the incident field with a known reference, and then shifting the reference by $\pi/2$. This will reveal the symmetric contribution to the phase (cosine) and the antisymmetric (sine) and reconstruct the field, including the phase. Using this technique, we can avoid the additional integration that emerges naturally in Eq.(B1). The first nonvanishing contribution is given by,

$$\mathcal{S}_{S;EE}\left(\omega_s,\omega_1,\omega_2,\boldsymbol{Q},T\right)=\kappa_2^{-1}\left\langle E\left[\omega_1;\Lambda\right]S^{[1]}\left(\omega_s,\boldsymbol{Q},T;\Lambda\right)E^*\left[\omega_2;\Lambda\right]\right\rangle_\Lambda,\tag{B9}$$

This signal results in a the phase exponent,

$$\left\langle e^{i\lambda(\varphi_{ab}^s-\varphi_{cb}^s+\varphi[\omega_1]-\varphi[\omega_2])}\right\rangle_\Lambda.$$

When the interval (ω_1,ω_2) does not overlap $(\omega_s+\omega_{ab},\omega_s+\omega_{cb})$, this can be factorized as,

$$\left\langle e^{i\lambda(\varphi_{ab}^s-\varphi_{cb}^s)}\right\rangle\left\langle e^{i\lambda\{\varphi[\omega_1]-\varphi[\omega_2]\}}\right\rangle=e^{-\lambda^2\sigma^2|\omega_{ca}|}e^{-\lambda^2\sigma^2|\omega_1-\omega_2|},\tag{B10}$$

which suppresses the temporal evolution even further. This can be eliminated by calculating the covariance, which recovers the phase mixing terms. We define the covariance signal as,

$$\begin{aligned}\mathcal{C}_{S;EE}\left(\omega_s,\omega_1,\omega_2,\boldsymbol{Q},T\right)&=\kappa_2^{-1}\left\langle E\left[\omega_1;\Lambda\right]S^{[1]}\left(\omega_s,\boldsymbol{Q},T;\Lambda\right)E^*\left[\omega_2;\Lambda\right]\right\rangle_\Lambda\\&-\kappa_2^{-1}\left\langle E\left[\omega_1;\Lambda\right]E^*\left[\omega_2;\Lambda\right]\right\rangle_\Lambda\left\langle S^{[1]}\left(\omega_s,\boldsymbol{Q},T;\Lambda\right)\right\rangle_\Lambda.\end{aligned}\tag{B11}$$

The ensemble average over the stochastic degrees of freedom yields,

$$\left\langle e^{i\lambda\{\varphi_{ab}^s-\varphi_{cb}^s-\varphi[\omega_1]+\varphi[\omega_2]\}}\right\rangle_\Lambda-\left\langle e^{i\lambda\{\varphi_{ab}^s-\varphi_{cb}^s\}}\right\rangle_\Lambda\left\langle e^{-i\lambda\{\varphi[\omega_1]-\varphi[\omega_2]\}}\right\rangle_\Lambda,\tag{B12}$$

this factor does not vanish when the integration interval (ω_1, ω_2) overlaps with $(\omega_s + \omega_{ab}, \omega_s + \omega_{cb})$, which results in the phase mixing contributions. Assuming $\omega_2 > \omega_1$ and $\omega_{ca} > 0$ (without loss of generality) we have,

$$\varphi^s_{ab} - \varphi^s_{cd} - \varphi\left[\omega_1\right] + \varphi\left[\omega_2\right] = \int_{\omega_s+\omega_{ab}}^{\omega_1} d\omega\phi - \int_{\omega_s+\omega_{cb}}^{\omega_2} d\omega\phi, \tag{B13}$$

where the sign flips when boundary frequencies cross. This will not change the correlation function that only depends on the the interval length. The overall correlation function then reads,

$$\mu_{abc}\left(\sigma\right) = \begin{cases} e^{-\lambda^2\sigma^2|\omega_1-\omega_s-\omega_{ab}|}e^{-\lambda^2\sigma^2|\omega_2-\omega_s-\omega_{cb}|}; & \omega_{ca} > 0 \\ e^{-\lambda^2\sigma^2|\omega_2-\omega_s-\omega_{ab}|}e^{-\lambda^2\sigma^2|\omega_1-\omega_s-\omega_{cb}|}; & \omega_{ca} < 0 \end{cases}. \tag{B14}$$

By tuning $\omega_1 = \omega_s + \omega_{ab}$ and $\omega_2 = \omega_s + \omega_{cb}$, one can probe the temporal dynamics around these two frequency windows of width $\propto 1/\lambda^2\sigma^2$.This demonstrates the frequency-time resolution tradeoff for noisy pulses. The overall signal reads,

$$\begin{aligned} \mathcal{C}_{S;EE}\left(\omega_s,\omega_1,\omega_2,\boldsymbol{Q},T\right) &= \kappa_2^{-1}\left\{\left\langle E\left[\omega_1;\Lambda\right]S^{[1]}\left(\omega_s,\boldsymbol{Q},T;\Lambda\right)E^*\left[\omega_2;\Lambda\right]\right\rangle_\Lambda - \left\langle E\left[\omega_1;\Lambda\right]E^*\left[\omega_2;\Lambda\right]\right\rangle_\Lambda\left\langle S^{[1]}\left(\omega_s,\boldsymbol{Q},T;\Lambda\right)\right\rangle_\Lambda\right\} \\ &= |\boldsymbol{A}^s|^2\,\mu_{ggg}\underbrace{|\sigma_{gg}\left(\boldsymbol{Q}\right)|^2}_{\text{(a)}} + \sum_e \mu_{geg}\left|\boldsymbol{A}^s_{ge}\right|^2\underbrace{|\sigma_{eg}\left(\boldsymbol{Q}\right)|^2}_{\text{(b)}} + \sum_{e_1e_2}\mu_{e_1ge_2}\boldsymbol{A}^s_{e_1g}\boldsymbol{A}^{s*}_{e_2g}\underbrace{\sigma_{e_1g}\left(\boldsymbol{Q}\right)\sigma^*_{e_2g}\left(\boldsymbol{Q}\right)}_{\text{(d)}}e^{i\omega_{e_1e_2}T} \\ &+ \sum_{e_1e_2e_3}\mu_{e_1e_2e_3}\boldsymbol{A}^s_{e_1e_2}\boldsymbol{A}^{s*}_{e_3e_2}\underbrace{\sigma_{e_1e_2}\left(\boldsymbol{Q}\right)\sigma^*_{e_3e_2}\left(\boldsymbol{Q}\right)}_{\text{(c)}}e^{i\omega_{e_1e_3}T} \\ &+ 2\mathfrak{Re}\left\{\sum_{e_1} e^{i\omega_{e_1g}T}\left[\mu_{e_1gg}\boldsymbol{A}^s_{e_1g}\boldsymbol{A}^{s*}_{gg}\underbrace{\sigma_{e_1g}\left(\boldsymbol{Q}\right)\sigma^*_{gg}\left(\boldsymbol{Q}\right)}_{\text{(e \& h)}} + \sum_{e_2}\mu_{e_1e_2g}\boldsymbol{A}^s_{e_1e_2}\boldsymbol{A}^{s*}_{ge_2}\underbrace{\sigma_{e_1e_2}\left(\boldsymbol{Q}\right)\sigma^*_{ge_2}\left(\boldsymbol{Q}\right)}_{\text{(f \& g)}}\right]\right\}. \end{aligned} \tag{B15}$$

We verify in this case that each contribution to the signal can be controlled by $\mu_{abc}\left(\sigma\right)$. Generally ω_1 and ω_2 can be chosen from different bands (or scales) such that the contribution by diagram can be explicitly written (mostly $\omega_{ca} > 0$ excluding the last two term),

$$\begin{cases} \mu_{ggg} = e^{-\lambda^2\sigma^2|\omega_1-\omega_s|}e^{-\lambda^2\sigma^2|\omega_2-\omega_s|}; & \text{a} \\ \mu_{geg} = e^{-\lambda^2\sigma^2|\omega_1-\omega_s-\omega_{ge}|}e^{-\lambda^2\sigma^2|\omega_2-\omega_s-\omega_{ge}|}; & \text{b} \\ \mu_{e_1e_2e_3} = e^{-\lambda^2\sigma^2\left|\omega_1-\omega_s-\omega_{e_1e_2}\right|}e^{-\lambda^2\sigma^2\left|\omega_2-\omega_s-\omega_{e_3e_2}\right|}; & \text{c}, e_1 < e_3 \\ \mu_{e_1ge_2} = e^{-\lambda^2\sigma^2\left|\omega_1-\omega_s-\omega_{e_1g}\right|}e^{-\lambda^2\sigma^2\left|\omega_2-\omega_s-\omega_{e_2g}\right|}; & \text{d}, e_1 < e_2 \\ \mu_{e_1gg} = e^{-\lambda^2\sigma^2\left|\omega_2-\omega_s-\omega_{e_1g}\right|}e^{-\lambda^2\sigma^2|\omega_1-\omega_s|}; & \text{(e \& h)} \\ \mu_{e_1e_2g} = e^{-\lambda^2\sigma^2\left|\omega_2-\omega_s-\omega_{e_1e_2}\right|}e^{-\lambda^2\sigma^2|\omega_1-\omega_s-\omega_{ge_2}|}; & \text{(f \& g)} \end{cases}. \tag{B16}$$

This is a demonstration of a possible combination for the correlation function used in Eq.(8) of the main text, one has to determine the contributions for $\omega_{ca} < 0$ as well.

[1] K. Bennett, J. D. Biggs, Y. Zhang, K. E. Dorfman, and S. Mukamel, Journal of Chemical Physics **140** (2014), 10.1063/1.4878377.

[2] K. Bennett, M. Kowalewski, J. R. Rouxel, and S. Mukamel, Proceedings of the National Academy of Sciences **115**, 6538 (2018).